Jan Havelka; Jan Sýkora
Application of Calderón's inverse problem in civil engineering

Applications of Mathematics, Vol. 63 (2018), No. 6, 687–712

Persistent URL: http://dml.cz/dmlcz/147564

63 (2018) APPLICATIONS OF MATHEMATICS No. 6, 687–712

APPLICATION OF CALDERÓN'S INVERSE PROBLEM IN CIVIL ENGINEERING

Jan Havelka, Jan Sýkora, Praha

Received November 20, 2017. Published online December 3, 2018.

Abstract. In specific fields of research such as preservation of historical buildings, medical imaging, geophysics and others, it is of particular interest to perform only a non-intrusive boundary measurements. The idea is to obtain comprehensive information about the material properties inside the considered domain while keeping the test sample intact. This paper is focused on such problems, i.e. synthesizing a physical model of interest with a boundary inverse value technique. The forward model is represented here by time dependent heat equation with transport parameters that are subsequently identified using a modified Calderón problem which is numerically solved by a regularized Gauss-Newton method. The proposed model setup is computationally verified for various domains, loading conditions and material distributions.

Keywords: Calderón problem; finite element method; diffusion equation; boundary inverse value method; Neumann-to-Dirichlet map

MSC 2010: 65M32, 35K05

1. Introduction

In this paper we propose a non-invasive parameter identification technique based merely on boundary observations of the object of interest. This idea was initially inspired by a medical imaging technique named Electric Impedance Tomography (EIT) which was first rigorously described by the Argentinian mathematician Alberto Calderón in his foundational paper [10] in 1980. The ultimate goal of EIT is to determine the electric conductivity field inside an object of interest using only boundary measurements. The basic idea of this method lies in the difference of surface measurements due to variations in the subsurface conductivity distribution.

The financial support of this research by the GA15-07299S and GA16-11473Y is gratefully acknowledged.

DOI: 10.21136/AM.2018.0323-17

While a single set of surface measurements for a given loading conditions might result in a number of possible conductivity fields, Calderón surpassed this problem by sequentially implying multiple loading conditions, for which the system responses have the potential to contain complete information about the underlying conductivity distribution.

We especially focus on physical models applicable in civil engineering, e.g. problems mainly governed by elliptic or parabolic partial differential equations (PDEs) with defined geometry, loading and material properties. Specifically we consider a single-parameter steady-state heat equation as a direct analogy to the standard use of Calderón inverse problem paradigm in electrostatics and a time dependent heat transport as a representative of a multi-parameter model. Such problems have been studied during past few years from several perspectives. Spatially distributed thermal conductivity for the steady-state heat equation was first estimated from boundary measurements in [19]. The defects or inhomogeneities in the thermal conductivity field were presented in [2] and [18]. More complex approach focused on the transient problem, i.e. identifying the thermal conductivity and the volumetric heat capacity, was introduced in [3] and [22]. The three dimensional aspects of parameter estimation for stationary and non-stationary heat problem were proposed in [41]. In this paper, we present a detailed insight into the concept of parameter identification and focus on the comparison of steady-state and transient model. Moreover, our proposed method considering a time dependent heat transport is designed to be an external loading-free method, i.e., it completely relies on the environmental factors as a source of changes which are necessary in order to identify the material properties inside the domain.

The paper is organised as follows: Section 2 comprises a thorough description of forward models, i.e., the physical meaning of individual elements, measuring techniques, boundary conditions and numerical solutions. In Section 3 we discuss a common approach to solving an inverse problems with an iterative regularized Gauss-Newton algorithm. Further, we also comment on implementation details which are necessary in order to ensure the stability of the solver. In Section 4 we give an overview of the identification algorithm performance, considering various scenarios, i.e., domain shapes, material distributions, loading conditions and limited number of measurement points. Our results are then summarized in the last section.

2. Forward models

Throughout this paper, we consider basically three numerical models which are based on diffusion equation. Computational models play a fundamental role, since each is repeatedly used in the inverse process and also for simulating the error-less data. Numerical solutions for each model are always based on the finite element method. The space and time discretization and other specifications are briefly outlined for each model within its section. All relevant information regarding the derivation, implementation and relationships of FEM principles proposed in this paper can be for example found in [4] and the literature therein.

Main ideas of employing Calderón's technique in foregoing models are created upon the foundational research conducted in [13], which proposed and experimentally validated so called *Complete Electrode Model* (CEM). In this model, electrodes are considered with their actual physical size with a contact impedance layer between the skin and the electrode.

In order to capture the shift from electrostatics to the heat transfer in terms of assumptions that lead to unique solutions, it is important to understand the basic features of the CEM which is defined as [35]

$$
\begin{cases}
\nabla \cdot (\sigma(x)\nabla v(x)) = 0, & x \in \Omega, \\
\displaystyle\int_{e_s} \sigma(x)\frac{\partial v}{\partial n}(x)\,\mathrm{d}S = I_s, & s = 1,\dots,m_s, \\
\sigma(x)\dfrac{\partial v}{\partial n}(x) = 0, & x \in \partial\Omega \setminus \displaystyle\bigcup_{s=1}^{m_s} e_s, \\
v(x) + z_s\sigma(x)\dfrac{\partial v}{\partial n}(x) = V_s, & x \in e_s,\ s = 1,\dots,m_s,
\end{cases}
\tag{2.1}
$$

where $\Omega \subseteq \mathbb{R}^d$, $d = 2$, is a bounded domain with a piecewise smooth boundary. The outward unit normal vector to the boundary is denoted by n. A known electrical conductivity σ is given on the closure of Ω. The model consists of m_s electrodes $(e_s)_{s=1}^{m_s}$ modelled as a part of the surface $\partial\Omega$, each with known contact impedances $(z_s)_{s=1}^{m_s}$ that are assumed to be constant. The current pattern applied to the electrodes is denoted by $(I_s)_{s=1}^{m_s} \in \mathbb{R}^{m_s}$. The electrostatic potential field within the domain is denoted by $v(x)$. The model conditions introduced in (2.1) can be translated as follows: the first term is the governing equation, the second condition indicates that the current flux is averaged across each electrode e_s and gives rise to a known (measured) constant current I_s. The third condition implies that there is no current leakage through the bare skin, assuming that the air is an insulator and the last term is a Robin condition, which includes z_s, a skin-electrode contact impedance. The problem in (2.1) determined by the first three equalities is solvable under some natural

assumptions such as the positiveness of σ and $\sum_{s=1}^{m_s} I_s = 0$. The latter condition also has a physical justification as conservation of charge. The fourth equality in (2.1) shows how the potential v determines the electrode potential V_s on each electrode e_s. Motivated by physical considerations, we can expect that V_s are constants. A question arises, whether problem (2.1) with unknown constants V_s has a solution. That is, whether a function v and a vector from $\mathbb{R}^{m_s}$ exist such that they solve (2.1).

In [35], the weak formulation of (2.1) was presented and the proof of the existence of a solution formed by v and $V = (V_1, \ldots, V_{m_s})$ was given under the following assumptions.

Assumption 2.1. The conductivity σ, the contact impedances z_s and the current pattern I_s satisfy

(i) $\sigma \in L^\infty(\Omega; \mathbb{R}), \quad \inf_{x\in\Omega} \sigma(x) = \sigma_- > 0,$

(ii) $0 < z_- \leqslant z_s \leqslant z_+ < \infty, \quad s = 1, \ldots, m_s,$

(iii) $\sum_{s=1}^{m_s} I_s = 0.$

However, the solution is only defined up to addition of a constant to both v and V. It is proved in [35] that the uniqueness of the solution is ensured if $\sum_{s=1}^{m_s} V_s = 0$. By virtue of the linearity of (2.1), this condition can be used (a) for the *ex post* normalization of v and V, (b) in the definition of a vector subspace where V is searched for, or (c) in the setting of the reference potential if the electrode voltages are measured as in identification problems. A detailed description of the problem and its treatment can be found in [42], [13], [43], and the literature therein.

The identification algorithm works as follows. Model (2.1) is provided with the measured input data, i.e., the fluxes I_s, impedances z_s, along with a chosen estimate of the conductivity field σ. The part of the output of the model which we are interested in is primarily the set of electrical potentials V_s for particular choice of the field σ. The identification algorithm then adjusts the field σ in such a way that it minimises an appropriate norm of the difference $(V_s - W_s)$, where W_s represents the error-less (measured) data stemming from an experiment.[1]

2.1. General Transport Model (GTM). Following the same principles, one can generalize the concept for arbitrary transport process governed by a diffusion equation. For the purpose of civil engineering application, we shall consider a steady-

[1] In the following text we will denote these variables as: $V_s = F(\sigma)$ and $W_s = \mathbf{u}_m$.

state heat equation with its boundary conditions in the form

$$
\begin{cases}
\nabla \cdot (\lambda_s(x)\nabla u_h(x)) = 0, \quad x \in \Omega, \\
\lambda_s(x)\dfrac{\partial u_h}{\partial n}(x) = f_N(x), \quad x \in \partial\Omega_N \setminus e_h, \\
\alpha(u_h(x) - u_0(x)) = \lambda_s(x)\dfrac{\partial u_h}{\partial n}(x), \quad x \in \partial\Omega_T \setminus e_h, \\
u_h(x) + r_h\lambda_s(x)\dfrac{\partial u_h}{\partial n}(x) = T_h, \quad x \in e_h,\ h = 1, \dots, m_h, \\
\partial\Omega = \partial\Omega_T \cup \partial\Omega_N.
\end{cases}
\tag{2.2}
$$

The formulation of (2.2) considers m_h solutions of the governing equation on the first line, which is a response to m_h different boundary conditions, i.e. individual heaters, represented by the Robin condition on the last line. In contrast to EIT, the potential $u_h(x)$ represents here the temperature field for hth loading condition, thus the electrodes e_h now transform into heaters which are capable of changing their temperature instead of the electric current[2]. The other variables include the thermal conductivity field $\lambda_s(x)$, the outward pointing unit normal vector n and the constants r_h and T_h representing the heater resistance coefficient and the heater temperature of the hth loading state, respectively. The environmental factors are: α the constant heat transfer coefficient, $u_0(x)$ the environmental temperature and $f_N(x)$ the prescribed flux. The $\partial\Omega$ is a boundary of the domain Ω. Note that T_h is a single constant for the hth out of m_h loading states indicating our intention to utilize a stimulation pattern in which only the hth heater is active while the others are inactive.

The inputs for this model are then the conductivity field $\lambda_s(x)$, the stimulation temperatures $(T_h)_{h=1}^{m_h}$, the contact resistances $(r_h)_{h=1}^{m_h}$ and the environmental factors α, $u_0(x)$ and $f_N(x)$. Subsequently, the model output consists of the temperature field $u(x)$ with its trace on the boundary $\partial\Omega$. In the numerical settings, m_h heaters, which are activated one by one, are attached to the boundary $\partial\Omega$. For each active heater one captures the temperature in m_n measurement nodes on the boundary $\Gamma_m \subseteq \partial\Omega$ forming a vector containing $m_h m_n$ numbers.

By simplifying Assumptions 2.1, the existence and uniqueness of the solution of the weak form of (2.2) is proved under the following assumptions, see [32].

Assumption 2.2. The conductivity $\lambda_s(x)$, the contact resistances r_h and the transfer coefficients α satisfy the following conditions:

[2] By using Robin condition together with the heater temperature T_h and transfer coefficient r_h, one can still employ the Neumann-to-Dirichlet map for GTM model, see Section 3.

(i) $\lambda_s \in L^\infty(\Omega;\mathbb{R}), \quad \inf\limits_{x\in\Omega} \lambda_s(x) = \lambda_s^+ > 0,$
(ii) $0 < r_h^- \leqslant r_h \leqslant r_h^+ < \infty, \quad h = 1,\dots,m_h,$
(iii) $0 < \alpha^- \leqslant \alpha \leqslant \alpha^+ < \infty.$

Note that in comparison to Assumption 2.1 there is no parallel to the condition for conservation of charge, i.e., $\sum I_s = 0$. By application of the second and the third equation in (2.2) the solution of the problem is unique and there is no need to introduce an analogy to the condition $\sum V_s = 0$ in CEM.

Unlike in EIT, where the measurements are conducted only by passive electrodes, one can actually choose all accessible parts of the boundary $\partial\Omega$, which can be understood as taking a thermal camera images. Because the stimulation temperatures T_h and resistances r_h for each heater are known a priori, the last equation in (2.2) can be interpreted as a prescribed flux with a reference temperature T_h, thus preserving the principle of loading with flux and measuring the potential at the boundary as it is common in EIT. The previously mentioned *current stimulation pattern* from EIT now translates into the *temperature stimulation pattern*, which can take nearly arbitrary form. Unlike in EIT, where at least two electrodes in each loading state must be active concurrently due to the third condition in Assumption 2.1, GTM is always provided with the reference temperature due to the third equation in (2.2), so one can stimulate the construction with just a single heater at time, which is also the case in our numerical examples.

Numerical solution of the forward model. The solution of (2.2) is obtained using the finite element method. The domain is discretized into N_e disjoint triangular elements with N_n nodes. The solution is approximated with $\varphi_i(x)$ for $i = 1,\dots,N_n$ linear basis functions. The parameter $\lambda_s(x)$ is approximated by an element-wise constant function and can be identified with a vector $\boldsymbol{\lambda}_s \in \mathbb{R}^{N_e}$.

In contrast to V_s in CEM, heater temperatures T_h in GTM are given a priori and the observed nodes on Γ_m that coincide with active heaters are excluded from the observation. Let us define the dependence of the nodal temperatures $u_h|_{\Gamma_m}$ on the parameter $\boldsymbol{\lambda}_s$ by the forward operator

$$\mathbf{F}(\boldsymbol{\lambda}_s) = \mathbf{u}_r, \quad \mathbf{u}_r \in \mathbb{R}^{m_n \cdot m_h}, \tag{2.3}$$

where $\mathbf{u}_r$ is the vector containing the temperatures on the boundary $\Gamma_m \subseteq \partial\Omega$ that is subjected to measurement, m_n is the cardinality of the discrete form of Γ_m, i.e. the number of FE nodes located on Γ_m and m_h is the number of heaters.

The full solution vector for the hth active heater $\mathbf{u}_h \in \mathbb{R}^{N_n}$, containing all temperatures in Ω, is obtained as

$$(\mathbf{K} + \mathbf{K}_t + \mathbf{K}_{e,h})\mathbf{u}_h = \mathbf{f}_t + \mathbf{f}_{e,h} + \mathbf{f}_n, \tag{2.4}$$

where the particular system matrices and corresponding right-hand side vectors are computed as

$$K_{jk} = \int_{\Omega} \lambda_s \nabla\varphi_j \cdot \nabla\varphi_k \,\mathrm{d}A, \quad j,k = 1,\dots,N_n, \tag{2.5}$$

$$K_{t,hjk} = \int_{\partial\Omega_T \setminus e_h} \alpha\varphi_j\varphi_k \,\mathrm{d}S, \quad j,k = 1,\dots,N_n,\ h = 1,\dots,m_h, \tag{2.6}$$

$$K_{e,hjk} = \int_{e_h} \frac{1}{r_h}\varphi_j\varphi_k \,\mathrm{d}S, \quad j,k = 1,\dots,N_n,\ h = 1,\dots,m_h, \tag{2.7}$$

$$f_{t,hj} = \int_{\partial\Omega_T \setminus e_h} \alpha u_0\varphi_j \,\mathrm{d}S, \quad j = 1,\dots,N_n,\ h = 1,\dots,m_h, \tag{2.8}$$

$$f_{e,h} = \int_{e_h} \frac{1}{r_h} T_h \,\mathrm{d}S, \quad h = 1,\dots,m_h, \tag{2.9}$$

$$f_{n,hj} = -\int_{\partial\Omega_N \setminus e_h} f_N\varphi_j \,\mathrm{d}S, \quad j = 1,\dots,N_n,\ h = 1,\dots,m_h. \tag{2.10}$$

2.2. Time dependent heat equation. In real conditions it is, however, not an easy task to maintain the steady-state conditions. Therefore, we intend to apply identical principles used in the Calderón problem for the time dependent model. To capture a time dependent heat transport, we adopt the following set of equations:

$$\begin{cases} \varrho_s(x)c_p(x)\dfrac{\partial u}{\partial t}(x,t) - \boldsymbol{\nabla}\cdot(\lambda_s(x)\boldsymbol{\nabla}u(x,t)) = 0, \quad x,t \in \Omega\times(0,t_s), \\ \lambda_s(x)\dfrac{\partial u}{\partial n}(x,t) = f_N(x,t), \quad x \in \partial\Omega_N, \\ \alpha(u(x,t) - u_0(x,t)) = \lambda_s(x)\dfrac{\partial u}{\partial n}(x,t), \quad x \in \partial\Omega_T, \\ \partial\Omega = \partial\Omega_N \cup \partial\Omega_T, \quad u(x,0) = 0 \quad \text{for } x \in \Omega, \end{cases} \tag{2.11}$$

where $\varrho_s(x)$ is the volumetric mass density, $c_p(x)$ is the specific heat capacity, t_s is the final time of the simulation and $\partial\Omega_{(N,T)}$ are the non-intersecting subsets of the boundary $\partial\Omega$ with corresponding environmental factors $u_0(x,t)$, α and $f_N(x,t)$. The solution existence and uniqueness of the weak form of (2.11) can be found in [24].

In the definition of this model in (2.11) one can notice that there is no mention of electrodes or heaters indicating our intention not to consciously intervene in the system itself, but only to rely on external influences and a natural fluctuation of the temperature. In situations, where the boundaries $\partial\Omega$ are not exposed to different external influences, one can adapt a similar techniques to GTM and CEM, i.e., to equip the boundary with a heater or cooler or control the ambient temperature using the second or the third condition in (2.11). From a practical point of view a special

feature of this model lies in its independence on the excitation device, i.e. stimulation electrodes or heaters, which manifests itself in a smaller requirements on the measuring equipment, i.e., the full measurement setup consists only of thermometer arrays or thermal cameras.

Numerical solution of the forward model. The discretization and approximation corresponds to the previous model with the extension to the volumetric capacity $c_v(x) = \varrho_s(x)c_p(x)$, which is approximated by piecewise constant functions on each element forming a vector $\mathbf{c}_v \in \mathbb{R}^{N_e}$. The forward operator $\mathbf{F}$ consists of two independent parameters and solves the system for chosen time steps m_t at once, giving rise to the formulation

$$\mathbf{F}(\boldsymbol{\lambda}_s, \mathbf{c}_v) = \mathbf{u}_r, \quad \mathbf{u}_r \in \mathbb{R}^{m_n \cdot m_t}, \tag{2.12}$$

where the inputs are the thermal conductivity $\boldsymbol{\lambda}_s$ and the volumetric capacity $\mathbf{c}_v$. The output of the forward operator is acquired as a subset of a full solution matrix[3] $\mathbf{u}_{\mathrm{sol}} = [\mathbf{u}_1, \mathbf{u}_2, \ldots, \mathbf{u}_{N_t}] \in \mathbb{R}^{N_n \times N_t}$, were N_t is the number of total time steps of the simulation, obtained from the set of linear equations

$$\begin{aligned}\mathbf{K}_C \mathbf{u}_{i+1} = (\mathbf{K}_C - \Delta t \widetilde{\mathbf{K}})\mathbf{u}_{i-1} + \Delta t((1-\tau)\mathbf{f}_{n,i-1} + \tau \mathbf{f}_{n,i}) + \ldots \\ + \Delta t((1-\tau)\mathbf{f}_{t,i-1} + \tau \mathbf{f}_{t,i}),\end{aligned} \tag{2.13}$$

$$\widetilde{\mathbf{K}} = \mathbf{K} + \mathbf{K}_t, \tag{2.14}$$

$$\mathbf{K}_C = \mathbf{C} + \tau \Delta t \widetilde{\mathbf{K}}, \tag{2.15}$$

where $\Delta t = t_{i+1} - t_i$ is the time step, $\tau \in \langle 0; 1 \rangle$ is a parameter[4], the system matrices and right-hand side vectors are computed in the following way:

$$K_{jk} = \int_\Omega \lambda_s \nabla \varphi_j \cdot \nabla \varphi_k \, \mathrm{d}A, \quad j,k = 1, \ldots, N_n, \tag{2.16}$$

$$C_{jk} = \int_\Omega \varrho_s c_p \varphi_j \varphi_k \, \mathrm{d}A, \quad j,k = 1, \ldots, N_n, \tag{2.17}$$

$$K_{t,jk} = \int_{\partial\Omega_T} \alpha \varphi_j \varphi_k \, \mathrm{d}S, \quad j,k = 1, \ldots, N_n, \tag{2.18}$$

$$f_{t,ji} = \int_{\partial\Omega_T} \alpha u_{0,i} \varphi_l \, \mathrm{d}S, \quad i = 1, \ldots, N_t, \ j = 1, \ldots, N_n, \tag{2.19}$$

$$f_{n,ji} = -\int_{\partial\Omega_N} f_N(t_i) \varphi_j \, \mathrm{d}S, \quad i = 1, \ldots, N_t, \ j = 1, \ldots, N_n. \tag{2.20}$$

[3] From which $m_n < N_n$ and $m_t \leqslant N_t$ numbers are utilized in the identification process.
[4] The foregoing computations were calculated by the Crank-Nicolson scheme, i.e. $\tau = 0.5$.

3. Inverse problem

In a classical concept of numerical analysis, one is often provided with an appropriate physical model and a certain surrounding environment, i.e., a set of possible causes with a knowledge of the system behaviour, determining the required model responses. Such procedure is called a forward model and is opposite to the inverse problem, for which the main objective is to determine the cause from a given set of observations. Generally, the majority of forward models for physical situations leads to well-posed problems in the sense of Hadamard, see [15], for which the conditions can be stated as:

- ▷ for all admissible data the solution exists (existence),
- ▷ for all admissible data there is at most one solution of the problem (uniqueness),
- ▷ the solution depends continuously on the data (stability).

However, inverse problems do not necessarily have the aforementioned properties. Solution of such problems might therefore not be unique or stable and even small changes in the input data can result in large changes in the solution violating the third condition, thus the problem can be recognised as ill-posed, see [42], [20]. Another criterion that comes into consideration is the uniqueness of solution which can be better understood as a possible information shortage or data insufficiency. Although lack of information cannot be remedied by any mathematical treatment, see [25], stability of the solution can be treated by various mathematical procedures. In the case that the instability is intrinsic property of the system itself and the problem cannot be reformulated, one needs to provide additional assumptions, e.g., some prior information, enforcing smoothness, preferring solution with the smallest norm, provide bounds to the unknown entity, etc. Procedures for determining the constraints are generally called regularization methods and within this paper we shall employ a deterministic approach.

Mathematically the Calderón inverse problem represents a non-linear and severely ill-posed problem (see [29]) of recovering the coefficient of divergence σ in a system of elliptic partial differential equations. For electrostatic EIT, the problem is modelled by the generalized Laplace equation with boundary conditions

$$\begin{cases} \nabla \cdot (\sigma \nabla u) = 0 & \text{in } \Omega, \\ \sigma \nabla u \cdot n = f & \text{on } \partial\Omega, \end{cases} \tag{3.1}$$

satisfying the conservation of charge $\int_{\partial\Omega} f \,\mathrm{d}S = 0$ and choice of the reference voltage $\int_{\partial\Omega} u \,\mathrm{d}S = 0$ providing the solution existence and uniqueness respectively, see [32]. The term $f \in H^{-1/2}(\partial\Omega)$ is a given current flux on the Lipschitz boundary $\partial\Omega$ and the induced potential lying in the Sobolev space $u \in H^1(\Omega)$ uniquely solves

the Neumann boundary value problem in a bounded domain $\Omega \subseteq \mathbb{R}^2$. The electrical conductivity $\sigma \in L^\infty(\Omega)$ is assumed to be scalar valued, strictly positive and bounded in Ω and n is the outward pointing unit normal vector.

The knowledge of the resulting trace of the potential $u \in H^{1/2}(\partial\Omega)$ then gives rise to the Neumann-to-Dirichlet (NTD) $\Lambda_\sigma\colon\ H^{-1/2}(\partial\Omega) \to H^{1/2}(\partial\Omega)$ map, which can be formally defined as

$$\Lambda_\sigma\colon\ (\sigma\nabla u)\cdot n|_{\partial\Omega} \mapsto u|_{\partial\Omega}. \tag{3.2}$$

In general, it is also possible to proceed in the opposite way, i.e., to prescribe the Dirichlet boundary condition $u|_{\partial\Omega}$ in (3.1) and infer the current flux $(\sigma\nabla u)\cdot n|_{\partial\Omega}$, which would refer to the Dirichlet-to-Neumann (DTN) map.

The problem of interest is then to ask whether the Cauchy data, i.e., the pair of potentials and fluxes on the boundary, determine the conductivity σ in Ω uniquely. The injectivity of the forward map and uniqueness were proven under variety of assumptions in [39], [30], [9] and states that

$$\Lambda_{\sigma_1} = \Lambda_{\sigma_2} \Rightarrow \sigma_1 = \sigma_2. \tag{3.3}$$

For detailed information about DTN and NTD maps, see [40].

3.1. General procedure. Since the numerical procedures for solving ill-posed and non-linear problems are mathematically identical for various tasks, the boundary inverse problem can therefore be solved in a number of ways. The traditional approach is to linearize the problem and subsequently use a regularization method to stabilize the solver. The resulting system can be evaluated iteratively by one of the family of Newton-type methods. The opportunity to perform regularization of the problem prior to the linearization or vice versa opens up a wide range of possible ways to solve such problem. The minimization problem is often stated as follows, with the first term representing the cost function and the second term being the regularization penalty:

$$\sigma_{\mathrm{rec}} = \arg\min_\sigma \|\mathbf{u}_m - \mathbf{F}(\sigma)\|_p + G(\sigma). \tag{3.4}$$

We will call $\mathbf{F}(\sigma)$ a forward operator containing the model responses for all loading states on the observed part of the boundary, $\mathbf{u}_m$ represents the error-less system response[5], p indicates l_p-norm, $G(\sigma)$ is the regularization functional introducing

[5] By this we mean that we utilize only virtual measurements calculated with a given material distribution σ_{true} which is then unknown in the identification procedure, i.e. $\mathbf{u}_m = F(\sigma_{\mathrm{true}})$.

additional constraints to the solution and σ_{rec} is the parameter field being identified, i.e., σ is a general parameter which in the following text will, for example, represent conductivity λ_s or volumetric capacity c_v.

Since the identification methods in various fields are pursuing different objectives, e.g., the interest in non-iterative methods is mostly driven by the necessity of fast and reliable identification algorithms generating real time visualizations in medical imaging [16], [36], whereas in geophysics [11], [26], [17], iterative algorithms providing generally refined solutions are more preferred. From a wide range of identification techniques used in EIT one can choose, e.g. moment methods [1], Calderón's approach [7], back-projection [33], [5], one-step Newton family methods [6], [28], [12], layer stripping [36], or a more recently developed scattering transform, i.e. $\overline{\partial}$ method [34], [21]. Since our problems are inherently time dependent and relatively slow, we do not pursue real time imaging, but rather prefer more precise solution which is in our case provided by iterative Newton-type methods based on the assumption of small perturbations of the parameter field. A typical choice of the regularization penalty term in (3.4) has the following form, see [42]:

$$G(\sigma) = \kappa^2 \|\mathrm{L}(\sigma - \sigma_r)\|_{l_2}^2, \tag{3.5}$$

where the hyper-parameter (regularization parameter) κ is controlling the trade-off between the solution stability, given constraints and the distance from the true solution. In our implementation it is adjusted in every iteration in order to get closer to the true solution, see (3.11) and (3.7). Additional prior assumptions are contained in the reference field σ_r, which represents some known and possibly non-smooth transitions of the unknown parameter, see [17]. A straightforward way of explaining the regularization operator L is such that it draws the solution towards its null space[6], i.e. $\ker(\mathrm{L})$. It might take the form of the first and second order differential operator, a weighted diagonal matrix to promote a sparse solution, see [14], Gaussian smoothing filter, see [8], or, without any knowledge of the system, the operator is often an identity.

3.2. Numerical solution of the inverse problem. All results in Section 4 share the same regularized Gauss-Newton (GN) iteration scheme in the form of (3.7) and (3.6). Also the numerical procedures within this section and Section 4 refer to the situation after discretization. In our settings, both terms in (3.4) are preferred to be l_2-norm due to the convenience for computational purposes and the

[6] In our numerical examples we only utilize operators whose null space is a constant field, i.e. solutions close to $\sigma = \sigma_r + c$, where $c \in \mathbb{R}$ is the constant shift of the field, are preferred in general.

preference of smooth solutions, see [27]. In such case, by combining the minimization scheme equation (3.4) for $p = 2$, the penalty term equation (3.5) and a Gauss-Newton approximation of Newton-Raphson multi-variable method, one can obtain the following iterative formula, see [42]:

$$\boldsymbol{\sigma}_{k+1} = \boldsymbol{\sigma}_k + \delta\boldsymbol{\sigma}_k, \tag{3.6}$$

$$\delta\boldsymbol{\sigma}_k = (\mathbf{J}_k^{\mathrm{T}}\mathbf{J}_k + \kappa_k^2\mathbf{R})^{-1}(\mathbf{J}_k^{\mathrm{T}}\delta\mathbf{u} - \kappa_k^2\mathbf{R}(\boldsymbol{\sigma}_k - \boldsymbol{\sigma}_r)), \tag{3.7}$$

where $\mathbf{J}_k \in \mathbb{R}^{(m_n \cdot v)\times N_e}$ is the Jacobian evaluated at $\boldsymbol{\sigma}_k \in \mathbb{R}^{N_e}$, $\delta\mathbf{u}$ is the vector containing the difference between the model response and error-less data, see (3.9), $\mathbf{R}$ is the matrix composed from the regularization operator in the form

$$\mathbf{R} = \mathbf{L}^{\mathrm{T}}\mathbf{L} \in \mathbb{R}^{N_e \times N_e}, \tag{3.8}$$

$$\delta\mathbf{u} = \mathbf{u}_m - \mathbf{F}(\boldsymbol{\sigma}_k) \in \mathbb{R}^{m_n \cdot v}, \tag{3.9}$$

where $\mathbf{F}(\boldsymbol{\sigma}) \in \mathbb{R}^{m_n \cdot v}$ represents the discrete NTD forward operator with m_n being the number of measurement points, i.e., the number of nodes of the FE mesh on a subset Γ_m of the boundary $\partial\Omega$ that is being observed, and v is the number of distinct loading states[7]. The a priori measured quantity containing the error-less data is stored in a vector $\mathbf{u}_m \in \mathbb{R}^{m_n \cdot v}$. If not mentioned otherwise, the reference field $\boldsymbol{\sigma}_r$ is dropped out by setting it to zero and the iteration starts with a unit vector $\boldsymbol{\sigma}_0 \in \mathbb{R}^{N_e}$. The matrix $\mathbf{L} \in \mathbb{R}^{N_e \times N_e}$ represents the discrete counterpart of the operator L from (3.5) and is obtained as

$$L_{ij} = \begin{cases} -N_e^{(i)} & \text{if } i = j, \\ 1 & \text{if } \mathrm{conn}(i,j) \wedge i \neq j \text{ for } i,j = 1,\ldots,N_e, \\ 0 & \text{otherwise,} \end{cases} \tag{3.10}$$

where $N_e^{(i)}$ is the number of elements attached by an edge to the ith element and function $\mathrm{conn}(i,j)$ is true if and only if the ith and jth element share the same edge. From our experience, the most stable choice of the hyper-parameter $\kappa_k \in \mathbb{R}_{>0}$ is the one used in the Levenberg-Marquardt regularization (LMR), see [31], which is gradually decreasing during the iteration and takes the form

$$\kappa_k = \max_{r,s} \hat{j}_{k,rs} \quad \text{for } r,s = 1,\ldots,N_e, \tag{3.11}$$

[7] For the steady-state model, v corresponds to the number of heaters m_h, whereas for the transient model, v is equal to the number of chosen time steps m_t.

where $\hat{j}_{k,rs}$ are the elements of the squared Jacobian matrix, i.e. $\hat{\mathbf{J}}_k = \mathbf{J}_k^{\mathrm{T}}\mathbf{J}_k$. The Jacobian $\mathbf{J}_k$ is updated in each iteration and its entries are calculated as

$$J_k^{(emn)} = \frac{\partial F(\sigma_k)_{mn}}{\partial \sigma_k^e} = \frac{\partial u_{mn}}{\partial \sigma_k^e}, \tag{3.12}$$

where $\mathbf{J}_k$ is numerically calculated for kth iteration, indices m and n correspond to the measurement nodes and loading states, respectively. Index e identifies a conductivity change on the eth FE element. For convenience of the calculation, the Jacobian is matricised along indices mn.

Note that for multi-parameter model the vector $\boldsymbol{\sigma}$ takes the form $\boldsymbol{\sigma} = [\boldsymbol{\sigma}^{(1)}, \boldsymbol{\sigma}^{(2)}, \ldots, \boldsymbol{\sigma}^{(N_p)}]^{\mathrm{T}} \in \mathbb{R}^{N_e N_p}$, where N_p is the number of distinct parameters associated with each of the elements and the matrix $\mathbf{R} = \mathbf{I} \otimes \mathbf{L}\mathbf{L}^{\mathrm{T}}$, where $\mathbf{I} \in \mathbb{R}^{N_p \times N_p}$, is the identity matrix and the symbol $\otimes$ is the Kronecker product indicating the mutual spatial independence of parameters.

Additional numerical treatment. As the GN iteration scheme in (3.7) is fairly simple and does not include any supplementary constraints, we introduce two operators which increased the stability and robustness of the results. The constraint defined for the strict positivity of the conductivity field during the iteration is treated with an ad-hoc algorithm which does not allow the occurrence of negative numbers in the solution and gives rise to a *positivity operator* T_p. The operator evaluated for the ith component of the vector $\boldsymbol{\sigma} \in \mathbb{R}^{N_e}$ is of the form

$$T_p(\sigma_i) = \begin{cases} \sigma_i & \text{if } \sigma_i > 0, \\ \hat{\varepsilon} & \text{if } \sigma_i \leqslant 0, \end{cases} \tag{3.13}$$

where $\hat{\varepsilon} = 0.01 \cdot \overline{\sigma}_0$ is chosen to be sufficiently small so it does not cause numerical problems and $\overline{\sigma}_0$ is the average value of the starting vector for the parameter being identified. Since the problem is inherently non-linear and the iteration scheme proceeds with non-restricted linear steps, we introduce a *cap operator* T_c as

$$T_c(\delta\sigma_i) = \begin{cases} \operatorname{sign}(\delta\sigma_i) \cdot c & \text{if } |\delta\sigma_i| > c, \\ \delta\sigma_i & \text{if } |\delta\sigma_i| \leqslant c, \end{cases} \tag{3.14}$$

where the coefficient c represents the maximum step size. In the numerical examples we set the coefficient to $c = 0.5 \cdot \overline{\sigma}_0$. The final modified GN iteration scheme, after applying (3.13) and (3.14) to (3.6), is expressed as

$$\boldsymbol{\sigma}_{k+1} = T_p(\boldsymbol{\sigma}_k + T_c(\delta\boldsymbol{\sigma}_k)). \tag{3.15}$$

In order to keep the calculation efficient, the identification algorithm stops when the maximum number of iterations is reached or one of the following convergence criteria is satisfied:

$$\frac{\|\mathbf{u}_m - \mathbf{F}(\boldsymbol{\sigma}_k)\|_2}{\|\mathbf{u}_m\|_2} \leqslant \varepsilon, \tag{3.16}$$

$$\frac{\|\boldsymbol{\sigma}_{k-1} - \boldsymbol{\sigma}_k\|_2}{\|\boldsymbol{\sigma}_k\|_2} \leqslant \varepsilon, \tag{3.17}$$

where $\boldsymbol{\sigma}_k$ is the material field in the kth iteration. From our experience we set the maximum number of iterations to 40 and the threshold error $\varepsilon = 10^{-6}$.

4. Results

In this section we provide an insight into the performance of the proposed identification algorithm under various conditions, i.e., considering domains of different shapes, limited number of measurements or loading conditions, partial data identification and distinct material properties. In order to enhance the representativeness and the impartiality of the computational framework, we consider two different finite element meshes, one for simulating the true temperature field and the second one for calculating the temperature field based on the identified thermal conductivity field. The measure of the identification algorithm performance is represented as

$$\varepsilon_p = \frac{\|\mathbf{p}_{\text{rec}} - \mathbf{p}_{\text{true}}\|_2}{\|\mathbf{p}_{\text{true}}\|_2}, \tag{4.1}$$

where $\mathbf{p}_{\text{rec}}$ is the vector containing the identified quantity and $\mathbf{p}_{\text{true}}$ is the vector containing the true, i.e. error-less quantity. However, the difference in FEM meshes for the error-less data and the identification process might cause the vector dimension mismatch. In the case of the measured quantity, i.e., the system responses, the measurement nodes coincide for both meshes. For the parameter being identified, a known function f, e.g., $\sigma(\mathbf{x}) = f(\mathbf{x})$, is utilized. To obtain the vector of error-less data σ_{true} on a mesh, we simply take $\sigma_i = f(\mathbf{x}_{c,i})$, where $\mathbf{x}_{c,i}$ are the centroid coordinates for the ith element. The identification algorithm is run on a different, finer mesh. In order to compare the identified piecewise constant σ with the true values (see (4.1) for $p = \sigma$), f at the centroids of the finer mesh is evaluated.

4.1. General transport model. In order to make the first example easy to understand, we start with the identification of the thermal conductivity field $\boldsymbol{\lambda}_s$ in the steady-state heat problem, i.e. (2.2). The heat transport is defined by the

general transport model and fully introduced in Section 2.1. We put emphasis on the obstacles arising in civil engineering problems such as a limited number of measurement nodes on the boundary, reduced number of heaters or discontinuous or non-differentiable material fields. We utilize two geometrical domains, i.e., circular and L-shaped domain, with their finite element discretization, measurement nodes and positions of heaters are shown in Figure 1. Measurement nodes are marked as asterisks and three heaters placed on the external side of the boundary are labelled by numbers from 1 to 3. The boundary conditions for circular domain according to the third equation in (2.2) are set as

$$\begin{aligned} \lambda_s(x)\frac{\partial u}{\partial n}(x)|_{\partial\Omega_1} &= 10(u(x)-30), \\ \lambda_s(x)\frac{\partial u}{\partial n}(x)|_{\partial\Omega_2} &= 10(u(x)-15), \end{aligned} \tag{4.2}$$

where $\partial\Omega = \bigcup_{i=1}^{2} \partial\Omega_i$ and the number of observation nodes is $m_n = 52$. For the L-shaped domain, the boundary conditions are set as

$$\begin{aligned} \lambda_s(x)\frac{\partial u}{\partial n}(x)|_{\partial\Omega_1} &= 10(u(x)-30), \\ \lambda_s(x)\frac{\partial u}{\partial n}(x)|_{\partial\Omega_2} &= 10(u(x)-15), \\ \lambda_s(x)\frac{\partial u}{\partial n}(x)|_{\partial\Omega_3} &= 0, \end{aligned} \tag{4.3}$$

where $\partial\Omega_T = \bigcup_{i=1}^{2} \partial\Omega_i$ is the union of the outer and inner corner segment of the boundary, $\partial\Omega_3 = \partial\Omega \setminus \partial\Omega_T$ and the number of measurement nodes is $m_n = 74$. The heater properties are expressed as

$$\begin{aligned} T_i &= 5\,[^\circ\mathrm{C}], \\ r_i &= 0.01\,[\mathrm{m\,K\,W^{-1}}] \quad \text{for } i = 1,2,3, \\ l_i &= 0.1\,[\mathrm{m}], \end{aligned} \tag{4.4}$$

where l_i is the length of the individual heater. In contrast to the classical EIT, heaters serve one purpose only, i.e., to excite different boundary conditions and do not collect any kind of data. The collection of error-less data is assumed to be conducted by a thermal camera or by an array of discrete thermometers with an appropriate interpolation providing continuous surface data. The true parameter fields in Figure 1(c) and 1(f) represent an artificial material including inhomogeneities.

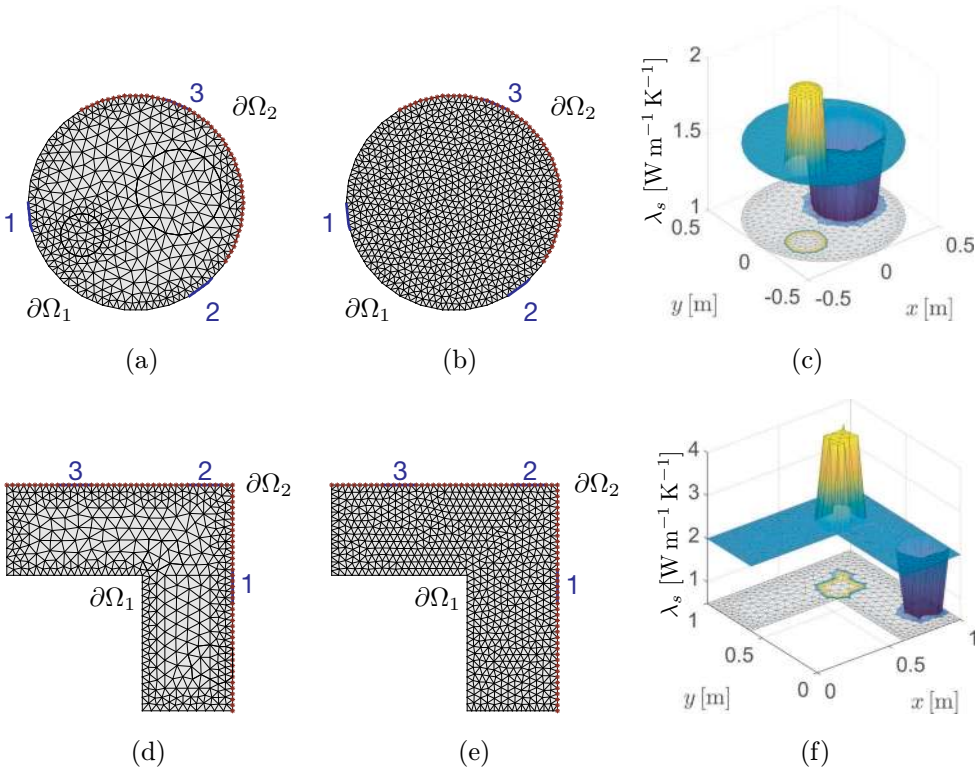

Figure 1. (a), (d) Domains utilized for simulating the measurement based on the true material field, (b), (e) domains used in the identification framework, (c), (f) the true material field—thermal conductivity.

In (3.4), the first term $\mathbf{u}_m$ is a vector of the measured quantity containing the error-less data. For both examples, we consider one observation of Γ_m for each of the $m_h = 3$ different heat loads. The measurement nodes representing the boundary Γ_m are labelled by asterisks, see Figure 1. The second term in (3.4) is the output of the forward operator $\mathbf{F}(\boldsymbol{\lambda}_s)$, i.e., the model response for the same loading conditions in the measurement nodes for a given thermal conductivity field. The first iteration starts with a spatially uniform thermal conductivity $\lambda_s = 1\,[\mathrm{W\,m^{-1}\,K^{-1}}]$.

The resulting fields showing the difference between the true and the identified thermal conductivity are depicted in Figure 2, where corresponding errors ε_{λ_s} and ε_T obtained from (4.1) are also presented.[8] Moreover, the errors ε_T which are summarized in the same figure are much smaller than ε_{λ_s} due to the smoothing effect of the stationary heat model.

[8] The error refers to the observed temperatures on the boundary, i.e. $u|_{\Gamma_m}$.

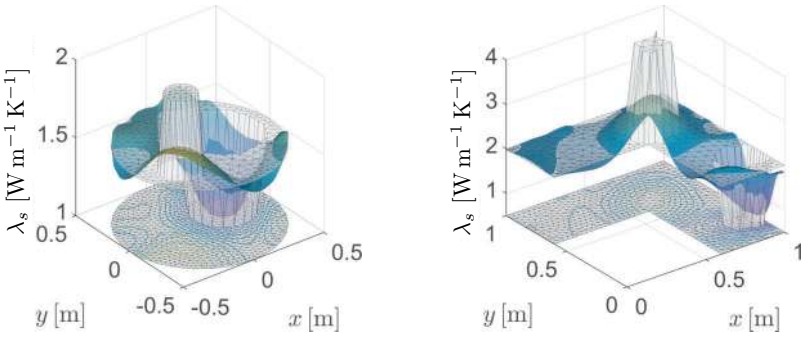

(a) (b)

Figure 2. (a) Circular domain—comparison of the true (transparent) and the identified (opaque) thermal conductivity field, $\varepsilon_{\lambda_s} = 0.0811$, $\varepsilon_T = 0.0038$, (b) L-shaped domain—comparison of the true and the identified thermal conductivity field, $\varepsilon_{\lambda_s} = 0.1732$, $\varepsilon_T = 0.0074$.

It can be seen that the obtained fields roughly correspond with the true fields. The most recognizable inaccuracies in the identified thermal conductivity field can be found in the close neighbourhood of the discontinuities and in general in regions with high frequency oscillations due to the smoothing effect of the governing equation, concrete choice of the operator L and the norm $p = 2$ in (3.4) also preferring smooth fields. Note that for increasing number of repeated measurements, i.e., sufficient number of loading states, the identified parameter field numerically converges to the true material field. However, such study is not the intent of the present paper and we refer the interested reader to [22]. We can finally conclude that the calculated results promote the capability of the proposed methodology to identify the material field from the boundary measurements for steady-state model.

4.2. Time dependent model. From a practical point of view, more interesting problem is represented by the time dependent heat equation, which can describe even sudden changes in external factors and loading conditions during the observation. In order to capture the transition from a steady-state heat transport to a transient problem, in the following example we put these two physical models in similar situation in terms of inputs. The examined L-shaped domain with measurement nodes, heaters and discretization[9] is depicted in Figure 3(a). The spatial distribution of the true material shown in Figure 3(b) and 3(c) does not correspond to a real building material and is deliberately chosen so that it is difficult to identify. The boundary conditions according to the second and the third equation in (2.11)

[9] The finite element mesh used in the identification algorithm is not shown.

are set as

$$\begin{aligned} \lambda_s(x)\frac{\partial u}{\partial n}(x,t)|_{\partial\Omega_1} &= 10(u(x,t)-25),\\ \lambda_s(x)\frac{\partial u}{\partial n}(x,t)|_{\partial\Omega_2\setminus(e_1\cup e_2)} &= 10(u(x,t)-5),\\ \lambda_s(x)\frac{\partial u}{\partial n}(x,t)|_{\partial\Omega_3} &= 0, \end{aligned} \tag{4.5}$$

where $\partial\Omega_T = \partial\Omega_1 \cup \partial\Omega_2$ is also used as the observed part of the boundary, i.e. $\Gamma_m = \partial\Omega_T$, and contains $m_n = 117$ nodes and $\partial\Omega_3 = \partial\Omega \setminus \partial\Omega_T$. The starting fields in the identification process are set according to the regular building materials as: $\lambda_s = 1\,[\mathrm{W\,m^{-1}\,K^{-1}}]$ and $c_v = 10^6\,[\mathrm{J\,m^{-3}\,K^{-1}}]$. The heater properties are set equivalently for both models. In particular, for steady-state model they are defined as

$$\begin{aligned} T_i &= 10 \quad [^\circ\mathrm{C}],\\ r_i &= 0.1 \quad [\mathrm{m\,K\,W^{-1}}] \quad \text{for} \quad i = 1,2,\\ l_i &= 0.1 \quad [\mathrm{m}], \end{aligned} \tag{4.6}$$

whereas for the transient model they are set as

$$\begin{aligned} \lambda_s(x)\frac{\partial u}{\partial n}(x,t)|_{e_1} &= 10(u(x,t)-T_1(t)),\\ \lambda_s(x)\frac{\partial u}{\partial n}(x,t)|_{e_2} &= 10(u(x,t)-T_2(t)). \end{aligned} \tag{4.7}$$

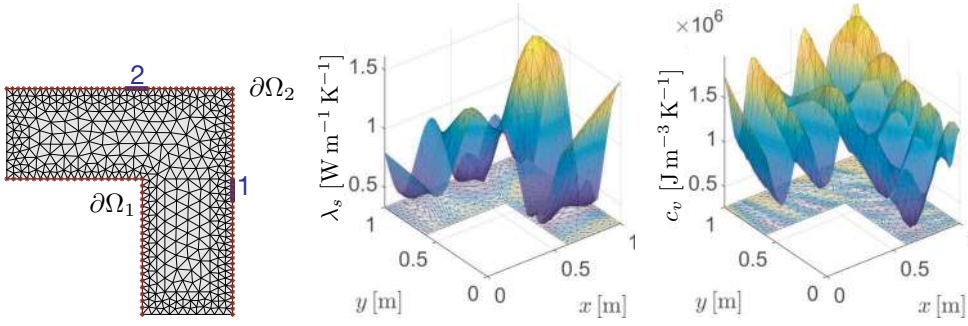

(a) (b) (c)

Figure 3. (a) L-shaped domain used for simulating real measurement, (b) the true material field—thermal conductivity, (c) the true material field—volumetric heat capacity.

The evolution of the temperature of individual heater $T_i\,[^\circ\mathrm{C}]$ and the corresponding model response $u_i\,[^\circ\mathrm{C}]$ in the domain underneath each heater is depicted in

Figure 4. This graphs primarily describe the temperature stimulation pattern employed for the transient problem. Each heater is consecutively excited to 10 [°C] for a single day with 12 hours shift between each loading condition, while the second heater is inactive. The collection of data starts from day two when the stationary state in Ω is approximately reached, i.e., the observation period lasts 3 days and the measurement of the temperature on the boundary Γ_m is recorded every two hours, i.e. $m_t = 36$, which overall yields 36×117 numbers.

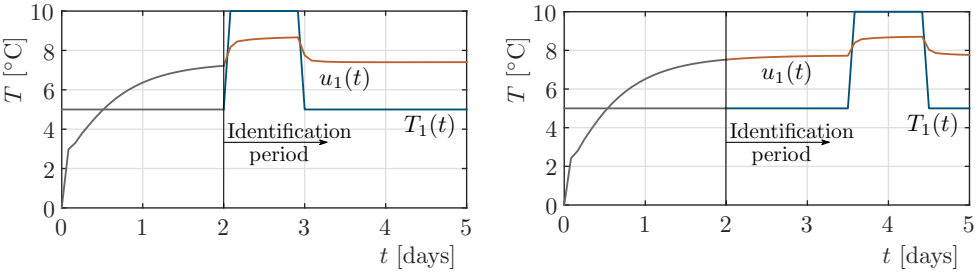

Figure 4. Prescribed temperatures for (a) the first and (b) the second heater.

Results for the stationary model are shown in Figure 5(a), while the identified fields for the time dependent model are shown in Figure 5(b) and 5(c). The identified fields visually correspond to the true fields and the conductivity λ_s for both models appears to be similar. However, both errors, i.e. ε_{λ_s} and ε_T, are a bit lower in the case of transient model in comparison to GTM. This is due to the fact that the transient model includes not only the approximate stationary data as well as GTM, but also additional data stemming from the transient problem.

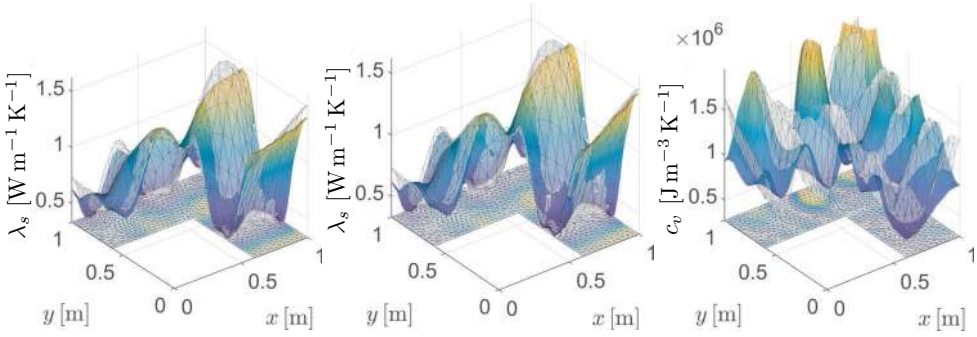

Figure 5. Comparison of the true (transparent) and the identified (opaque) field: (a) stationary problem—thermal conductivity field, $\varepsilon_{\lambda_s} = 0.0897$, $\varepsilon_T = 0.0009$, (b) transient problem—thermal conductivity field, $\varepsilon_{\lambda_s} = 0.0755$, $\varepsilon_T = 0.0006$, (c) transient problem—volumetric heat capacity, $\varepsilon_{c_v} = 0.2435$.

In the next example, we will take a look at a situation where the transient model is subjected to constant boundary conditions given by (4.8) for such a period of time for which the steady-state in the domain Ω is approximately reached. We will then gradually add individual time steps from the experiment to the identification algorithm and monitor the effect of the lack of data on the identified fields. The experiment is set in the following way: we utilize identical domain[10], discretization, measurement nodes and the true material field distribution as shown in Figure 3. The observation period starts from day 0 with an initial condition $u(x, t = 0) = 0$ for $x \in \Omega$ and lasts 2 days with 2 hour intervals, i.e., the total number of time steps is $N_t = 24$,

$$\begin{aligned} \lambda_s(x)\frac{\partial u}{\partial n}(x,t)|_{\partial\Omega_1} &= 10\,(u(x,t) - 25), \\ \lambda_s(x)\frac{\partial u}{\partial n}(x,t)|_{\partial\Omega_2} &= 10\,(u(x,t) - 5), \\ \lambda_s(x)\frac{\partial u}{\partial n}(x,t)|_{\partial\Omega_3} &= 0. \end{aligned} \tag{4.8}$$

As a measure of how close the data are to the stationary state, we utilize the formula

$$c_{st} = 1 - \frac{\|\mathbf{u}_s - \mathbf{u}_{n_t}\|_2}{\|\mathbf{u}_s\|_2}, \tag{4.9}$$

where $\mathbf{u}_s \in \mathbb{R}^{N_n}$ is the full solution vector calculated for the steady-state heat equation, N_n is the number of finite element nodes and $\mathbf{u}_{n_t} \in \mathbb{R}^{N_n}$ is the solution vector for the transient model evaluated at time step n_t. Most importantly, both vectors are evaluated for the true, i.e., error-less material parameters. The coefficient c_{st} serves only as an indication of how close the data from transient model are to the steady-state.

The following figure shows the relation between the error for both parameter fields calculated using (4.1) and the number of time steps $m_t = n_t$ given to the identification algorithm. It can be seen that involving more time steps into the identification is beneficial and any additional information leads to a more accurate identification of both fields. On the other hand, as the temperature develops over the time and approaches the steady-state, the error decreases more slowly, which is more pronounced in the error ε_{c_v} for the volumetric capacity. This is due to the fact that successful identification of volumetric capacity mainly depends on the time change of the temperature field, which becomes negligible towards the steady-state. Moreover, one can notice that even in the early stages of the evolution process, i.e. $m_t \leqslant 5$, the algorithm performs surprisingly well and despite only limited number

[10] With exception of heaters, which are not utilized in this example.

of observations m_t, it is able to identify at least a rough distribution of the true field, see Figures 6 and 7.

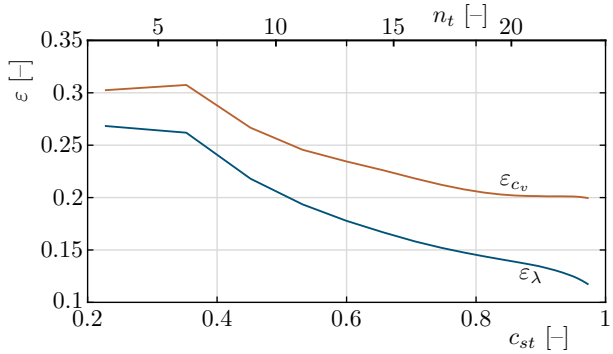

Figure 6. Material field errors calculated for different number of time steps involved in the calculation.

$n_t = 2$, $c_{st} = 0.2282$ $n_t = 8$, $c_{st} = 0.7052$ $n_t = 14$, $c_{st} = 0.8798$

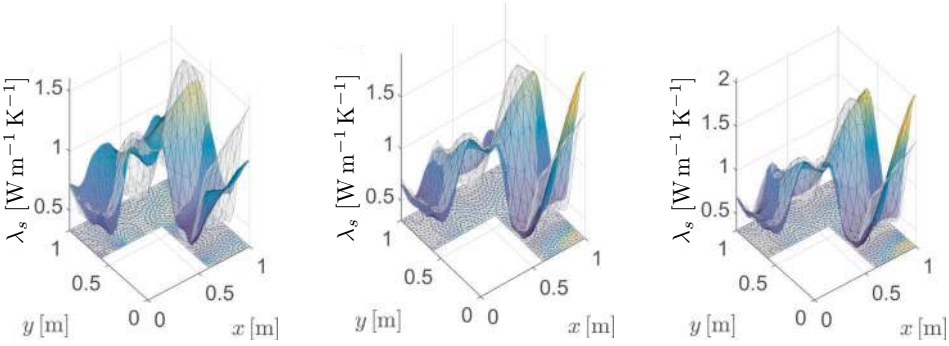

(a) $\varepsilon_{\lambda_s} = 0.2683$ (b) $\varepsilon_{\lambda_s} = 0.1582$ (c) $\varepsilon_{\lambda_s} = 0.1366$

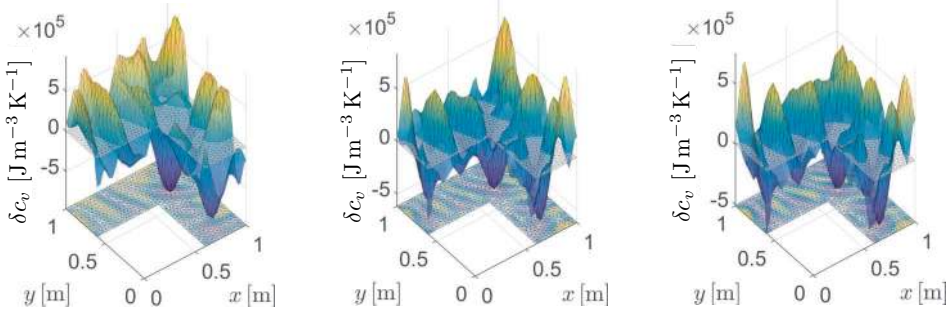

(d) $\varepsilon_{c_v} = 0.3025$ (e) $\varepsilon_{c_v} = 0.2183$ (f) $\varepsilon_{c_v} = 0.2015$

Figure 7. Samples of identified fields for 2, 8, and 14 time steps $m_t = n_t$. The second row shows the difference between the true (see Figure 3(c)) and the identified field.

The last example presents the capability of the identification framework when simulating the time dependent problem. We utilize identical domain shape and discretization as in the previous example, see Figure 3(a). In order to simulate a realistic environmental conditions and capture the temperature fluctuations in the interior and exterior, the heater elements in Figure 3(a) are omitted and a measurement using an arduino based weather station is conducted. The environment is in total monitored for eleven consecutive days at minute intervals. For computational purposes, the data were further sparsified to one hour intervals which satisfy both sufficient precision in describing the temperature curve and reasonable computational load. The resulting graphs without any additional processing are displayed in Figure 8.

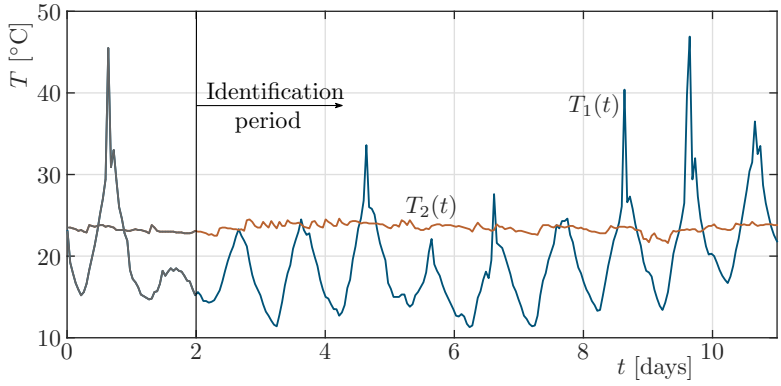

Figure 8. Interior (T_2) and exterior (T_1) temperatures, data included in the calculation spans from day 2 to 11.

The boundary conditions are set as

$$\begin{aligned} \lambda_s(x)\frac{\partial u}{\partial n}(x,t)|_{\partial\Omega_1} &= 10\,(u(x,t)-T_1(t)),\\ \lambda_s(x)\frac{\partial u}{\partial n}(x,t)|_{\partial\Omega_2} &= 10\,(u(x,t)-T_2(t)),\\ \lambda_s(x)\frac{\partial u}{\partial n}(x,t)|_{\partial\Omega_3} &= 0, \end{aligned} \tag{4.10}$$

where the environmental temperatures $T_1(t)$ and $T_2(t)$ are shown in Figure 8. Since the true material fields are identical to the ones in the previous example, see Figure 3(b) and 3(c), the starting fields for the first iteration are set in the same way, i.e. $\lambda_s = 1\,[\mathrm{W\,m^{-1}\,K^{-1}}]$ and $c_v = 10^6\,[\mathrm{J\,m^{-3}\,K^{-1}}]$. The observation period lasts 9 days and starts from day two with hourly intervals, which yields $m_t = 216$ observations. The observed part of the boundary Γ_m coincides with $\partial\Omega_1$ and $\partial\Omega_2$ and contains in total $m_n = 117$ nodes. The resulting identified fields are shown in the following figure.

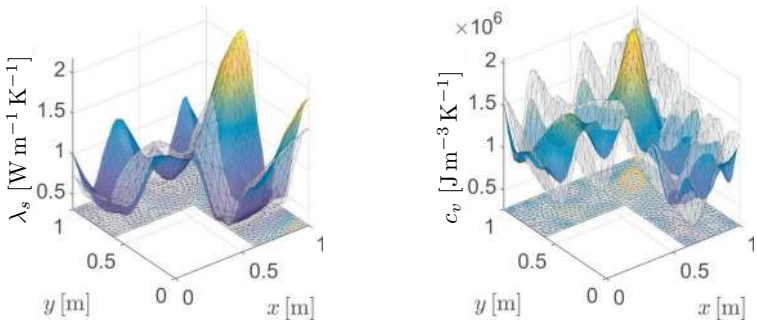

(a) (b)

Figure 9. (a) Comparison of the true (transparent) and the identified (opaque) thermal conductivity field, $\varepsilon_{\lambda_s} = 0.2074$, $\varepsilon_T = 0.0010$, (b) comparison of the true and the identified volumetric heat capacity, $\varepsilon_{c_v} = 0.2792$.

5. Conclusions

In this paper we have shown the possibilities of identifying material fields by using only boundary non-invasive measurements. Following the same principles as in the Calderón's inverse problem, we developed a steady-state model applicable in civil engineering, namely the heat transfer problem, which is comparable to a classical use of the electrical impedance tomography in the medical science. Moreover, we focused our attention on a more attractive issue which is the transient problem in heat transport. The identification procedure for non-stationary model is first compared to a steady-state problem with identical inputs and subsequently subjected to real climatic environment. The solver never failed. In all computational tests, the error of the observed temperatures and the identified parameter/s have been steadily decreasing during the iterations. However, one can spot noticeable inaccuracies in the identification of the volumetric capacity, which tends to have higher error in comparison to the conductivity field, see e.g. Figures 5, 7 and 9 and errors ε_{c_v} and ε_{λ_s} in the corresponding captions.

In oppose to electrical impedance tomography, where the crucial part of successful material field identification is based on a precise position of the measurement electrodes together with the boundary shape and knowledge of the loading conditions[11], in our application the problems might arise from insufficient space-time variability of environmental factors leading to imperfections and unwanted artefacts in the identified fields. In continuation of this work we intend to study the mutual ratio of terms

[11] Especially in the electrical impedance tomography, where the electrodes are placed on a human body, the boundary shape and electrodes are in continuous motion due to the patient breath and movement.

$\varrho_s c_p \partial u/\partial t$ and $\boldsymbol{\nabla} \cdot (\lambda_s \boldsymbol{\nabla} u)$ in (2.11) and its influence on the identified fields. In our opinion, the representation of both terms, expressed by the mutual ratio, is essential information when determining the ability to identify individual fields.

A further extension of the presented strategy would be the identification of the parameter fields for coupled heat and moisture problem. Supported by several successful studies of authors in the field of multi-scale simulations [38], uncertainty propagation [23], and modelling of degradation processes [37], we will adopt Künzel's diffusion model, because it is (i) relatively simple as it involves only a handful of material parameters, (ii) sufficiently accurate to describe the behaviour of structures under regular operation conditions, but is still (iii) complex enough to demonstrate the feasibility of the developed methodology towards the real-world applications.

A c k n o w l e d g e m e n t. The authors wish to acknowledge Prof. Hermann G. Matthies, Ph.D., for providing the knowledge base.

References

[1] *A. Allers, F. Santosa*: Stability and resolution analysis of a linearized problem in electrical impedance tomography. Inverse Probl. *7* (1991), 515–533. zbl MR doi
[2] *V. F. Bakirov, R. A. Kline, W. P. Winfree*: Discrete variable thermal tomography. AIP Conf. Proc. *700* (2004), 469–476. doi
[3] *V. F. Bakirov, R. A. Kline, W. P. Winfree*: Multiparameter thermal tomography. AIP Conf. Proc. *700* (2004), 461–468. doi
[4] *K.-J. Bathe*: Finite Element Procedures. Prentice Hall, Upper Saddle River, 2006.
[5] *C. A. Berenstein, E. Casadio Tarabusi*: Inversion formulas for the k-dimensional Radon transform in real hyperbolic spaces. Duke Math. J. *62* (1991), 613–631. zbl MR doi
[6] *R. S. Blue*: Real-time three-dimensional electrical impedance tomography. Ph.D. Dissertation, R.P.I, Troy, 1997.
[7] *R. S. Blue, D. Isaacson, J. C. Newell*: Real-time three-dimensional electrical impedance imaging. Physiological Measurement *21* (2000), 15–26. doi
[8] *A. Borsic, W. R. B. Lionheart, C. N. McLeod*: Generation of anisotropic-smoothness regularization filters for EIT. IEEE Transactions on Medical Imaging *21* (2002), 579–587. doi
[9] *R. M. Brown, G. A. Uhlmann*: Uniqueness in the inverse conductivity problem for nonsmooth conductivities in two dimensions. Commun. Partial Differ. Equations *22* (1997), 1009–1027. zbl MR doi
[10] *A. P. Calderón*: On an inverse boundary value problem. Comput. Appl. Math. *25* (2006), 133–138. zbl MR doi
[11] *S. Campana, S. Piro*: Seeing the Unseen. Geophysics and Landscape Archaeology. CRC Press, London, 2008. doi
[12] *M. Cheney, D. Isaacson, J. C. Newell, S. Simske, J. Goble*: NOSER: An algorithm for solving the inverse conductivity problem. Int. J. Imaging Systems and Technology *2* (1990), 66–75. doi
[13] *K.-S. Cheng, D. Isaacson, J. C. Newell, D. G. Gisser*: Electrode models for electric current computed tomography. IEEE Transactions on Biomedical Engineering *36* (1989), 918–924. doi
[14] *T. Dai, A. Adler*: Electrical Impedance Tomography reconstruction using l_1 norms for data and image terms. Conf. Proc. IEEE Eng. Med. Biol. Soc. *2008* (2008), 2721–2724. doi

[15] *C. W. Groetsch*: Inverse Problems in the Mathematical Sciences. Vieweg Mathematics for Scientists and Engineers, Vieweg, Braunschweig, 1993. zbl MR doi

[16] *S. J. Hamilton, M. Lassas, S. Siltanen*: A direct reconstruction method for anisotropic electrical impedance tomography. Inverse Probl. *30* (2014), Article ID 075007, 33 pages. zbl MR doi

[17] *D. S. Holder*: Electrical Impedance Tomography: Methods, History and Applications. Series in Medical Physics and Biomedical Engineering, Taylor & Francis, Portland, 2004.

[18] *C.-H. Huang, S.-C. Chin*: A two-dimensional inverse problem in imaging the thermal conductivity of a non-homogeneous medium. Int. J. Heat Mass Transfer *43* (2000), 4061–4071. zbl doi

[19] *M. R. Jones, A. Tezuka, Y. Yamada*: Thermal tomographic detection of inhomogeneities. J. Heat Transfer *117* (1995), 969–975. doi

[20] *A. Kirsch*: An Introduction to the Mathematical Theory of Inverse Problems. Applied Mathematical Sciences 120, Springer, New York, 2011. zbl MR doi

[21] *K. Knudsen, M. Lassas, J. L. Mueller, S. Siltanen*: Regularized D-bar method for the inverse conductivity problem. Inverse Probl. Imaging *3* (2009), 599–624. zbl MR doi

[22] *V. Kolehmainen, J. P. Kaipio, H. R. B. Orlande*: Reconstruction of thermal conductivity and heat capacity using a tomographic approach. Int. J. Heat Mass Transfer *51* (2008), 1866–1876. zbl doi

[23] *A. Kučerová, J. Sýkora, B. Rosić, H. G. Matthies*: Acceleration of uncertainty updating in the description of transport processes in heterogeneous materials. J. Comput. Appl. Math. *236* (2012), 4862–4872. zbl MR doi

[24] *O. A. Ladyženskaja, V. A. Solonnikov, N. N. Ural'ceva*: Linear and Quasi-Linear Equations of Parabolic Type. Translations of Mathematical Monographs 23, American Mathematical Society, Providence, 1968. zbl MR doi

[25] *C. Lanczos*: Linear Differential Operators. Classics in Applied Mathematics 18, Society for Industrial and Applied Mathematics, Philadelphia, 1996. zbl MR doi

[26] *R. E. Langer*: An inverse problem in differential equations. Bull. Am. Math. Soc. *39* (1933), 814–820. zbl MR doi

[27] *Y. Mamatjan, A. Borsic, D. Gürsoy, A. Adler*: Experimental/clinical evaluation of EIT image reconstruction with l_1 data and image norms. J. Phys., Conf. Ser. *434* (2013), 1–4. doi

[28] *J. L. Mueller, D. Isaacson, J. C. Newell*: Reconstruction of conductivity changes due to ventilation and perfusion from EIT data collected on a rectangular electrode array. Physiological Measurement *22* (2001), 97–106. doi

[29] *J. L. Mueller, S. Siltanen*: Direct reconstructions of conductivities from boundary measurements. SIAM J. Sci. Comput. *24* (2003), 1232–1266. zbl MR doi

[30] *A. I. Nachman*: Global uniqueness for a two-dimensional inverse boundary value problem. Ann. Math. (2) *143* (1996), 71–96. zbl MR doi

[31] *H. Niu, P. Guo, L. Ji, Q. Zhao, T. Jiang*: Improving image quality of diffuse optical tomography with a projection-error-based adaptive regularization method. Optics Express *16* (2008), 12423–12434. doi

[32] *K. Rektorys*: Variational Methods in Mathematics, Science and Engineering. D. Reidel Publishing Company, Dordrecht, 1980. zbl MR

[33] *F. Santosa, M. Vogelius*: A backprojection algorithm for electrical impedance imaging. SIAM J. Appl. Math. *50* (1990), 216–243. zbl MR doi

[34] *S. Siltanen, J. Mueller, D. Isaacson*: An implementation of the reconstruction algorithm of A. Nachman for the 2D inverse conductivity problem. Inverse Probl. *16* (2000), 681–699; erratum ibid. *17* (2001), 1561–1563. zbl MR doi

[35] *E. Somersalo, M. Cheney, D. Isaacson*: Existence and uniqueness for electrode models for electric current computed tomography. SIAM J. Appl. Math. *52* (1992), 1023–1040. zbl MR doi
[36] *E. Somersalo, M. Cheney, D. Isaacson, E. Isaacson*: Layer stripping: a direct numerical method for impedance imaging. Inverse Probl. *7* (1991), 899–926. zbl MR doi
[37] *J. Sýkora*: Modeling of degradation processes in historical mortars. Adv. Eng. Softw. *70* (2014), 203–212. doi
[38] *J. Sýkora, T. Krejčí, J. Kruis, M. Šejnoha*: Computational homogenization of non-stationary transport processes in masonry structures. J. Comput. Appl. Math. *236* (2012), 4745–4755. zbl doi
[39] *J. Sylvester, G. Uhlmann*: A global uniqueness theorem for an inverse boundary value problem. Ann. Math. (2) *125* (1987), 153–169. zbl MR doi
[40] *J. Syren*: Theoretical and numerical analysis of the Dirichlet-to-Neumann map in EIT. Master Thesis, University of Helsinki, 2016.
[41] *J. M. Toivanen, T. Tarvainen, J. M. J. Huttunen, T. Savolainen, H. R. B. Orlande, J. P. Kaipio, V. Kolehmainen*: 3D thermal tomography with experimental measurement data. Int. J. Heat Mass Transfer *78* (2014), 1126–1134. doi
[42] *M. Vauhkonen*: Electrical impedance tomography and prior information. Ph.D. Dissertation, Kuopio University, Joensuu, 2007.
[43] *M. Vauhkonen, W. R. B. Lionheart, L. M. Heikkinen, P. J. Vauhkonen, J. P. Kaipio*: A MATLAB package for the EIDORS project to reconstruct two-dimensional EIT images. Physiological Measurement *22* (2001), 107–111. doi

Authors' address: *Jan Havelka*, *Jan Sýkora*, Czech Technical University in Prague, Faculty of Civil Engineering, Deparment of Mechanics, Thákurova 7, 166 29 Praha 6, Czech Republic, e-mail: `jan.havelka.1@fsv.cvut.cz`, `jan.sykora.1@fsv.cvut.cz`.